A Monitoring Method Integrating Terrestrial Laser Scanning and Unmanned Aerial Vehicles for Different Landslide Deformation Patterns

Nan Jiang, Haibo Li, Yuxiang Hu, Jieyuan Zhang, Wei Dai, Congjiang Li, and Jia-Wen Zhou

***Abstract*—The three-dimensional deformation monitoring of landslides is very complex due to the uncertainty of movement direction and the difficulty in searching the corresponding points before and after deformation. In this study, a landslide deformation monitoring method based on the integration of terrestrial laser scanning (TLS) and unmanned aerial vehicles (UAVs) is presented. This method can quickly obtain high-precision and large-scale terrain information in the absence of sufficient ground control points (GCPs) and can accurately describe the real movement of landslides. The real-time kinematic (RTK) and post-processed kinematic (PPK) are applied to localize the initial positions of TLS and UAV, respectively. The iterative closest point algorithm is applied to register the TLS and UAV point cloud data. Then, the RTK-based GCPs and TLS-based GCPs are obtained to improve the accuracy of UAV data. After that, 3D deformation analyses based on shortest distance method and horizontal deformation based on the difference of orthophotos are applied through point clouds and orthophotos. The proposed method is demonstrated by monitoring a reactivated ancient landslide (Aniangzhai) in Danba County, Southwest China. The real deformation of the landslide has been validated with the registered TLS data. The results indicate that the downcutting of the riverbed and erosion to the slope toe caused by the dam break flood are the main reasons for the reactivation.**

***Index Terms*—Ancient landslide, data fusion, deformation analysis, monitoring method, reactivation mechanism, remote sensing.**

I. Introduction

THE reactivation of ancient landslides refers to the remobilization of landslide deposits in response to triggering factors such as earthquakes, long-term rainfall, groundwater erosion, and human activities [1], [2]. Compared with the rock avalanche or collapse, reactivated landslides usually have a slow deformation rate and a long duration [3], [4]. The in-depth understanding of the inducing factors, initiating mechanism, and movement process of reactivated ancient landslides is significant for early identification and emergency treatment of landslide risks [5], [6]. For mountainous cities, towns, and villages with potential landslide risks and large populations, monitoring the process of landslide movement is an important part of risk management [7], [8].

Traditional capabilities for monitoring landslides include single-point devices such as crack monitoring devices, global navigation satellite system (GNSS), and total station [9]. These sensors or devices reflect the landslide movement by recording the relative or absolute displacement of monitoring points [10]. Although the accuracy of these traditional monitoring methods is relatively high, their monitoring range is limited by the number and distribution of monitoring devices. This makes them more suitable for local high-precision landslide deformation monitoring than for reflecting the overall deformation characteristics of large-scale landslides [11]. In recent years, with the rapid development of remote sensing technologies, it is possible to obtain large-scale terrain information to detect/monitor landslides in a wider scope. These remote sensing technologies can be divided into three categories according to their platforms: spaceborne high-resolution satellite [12] and Synthetic Aperture Radar (SAR) [13], airborne unmanned aerial vehicle (UAV) photogrammetry [14], and light detection and ranging [15], and ground-based devices such as ground-based interferometric SAR (GB-SAR) [16] and terrestrial laser scanning (TLS) [17]. Among them, the spaceborne technologies have been proved to be effective in large-scale landslide hazard identification, deformation monitoring, and landslide sensitivity analysis [18]–[22]. Nevertheless, they cannot match the spatial detail or time resolution achievable by means of airborne or ground-based devices [23]. For example, GB-SAR can accurately identify the slope deformation of a few millimeters in several seconds [24], and the distance between the point clouds obtained by TLS can reach a few millimeters [25], [26]. Comparatively, the monitoring range and accuracy of airborne remote sensing technologies are between the spaceborne and ground-based devices [27], and the flexibility and high adaptability to complex terrain make it play an irreplaceable role in data acquisition, deformation monitoring, and landslide susceptibility mapping [28]–[32].

Manuscript received May 16, 2021; revised July 13, 2021, August 16, 2021, and September 23, 2021; accepted October 2, 2021. Date of publication October 6, 2021; date of current version October 21, 2021. This work was supported in part by the National Key R&D Program of China under Grant 2017YFC1501102, in part by the National Natural Science Foundation of China under Grant U20A20111 and Grant 41977229, and in part by the Sichuan Youth Science and Technology Innovation Research Team Project under Grant 2020JDTD0006. *(Corresponding author: Jia-Wen Zhou.)*

Nan Jiang, Haibo Li, Yuxiang Hu, and Jia-Wen Zhou are with the State Key Laboratory of Hydraulics and Mountain River Engineering, Sichuan University, Chengdu 610065, China (e-mail: 2018223060073@stu.scu.edu.cn; hbli@scu.edu.cn; 2020323060046@stu.scu.edu.cn; jwzhou@scu.edu.cn).

Jieyuan Zhang, Wei Dai, and Congjiang Li are with the College of Water Resource and Hydropower, Sichuan University, Chengdu 610065, China (e-mail: 2019223060084@stu.scu.edu.cn; 2020223065127@stu.scu.edu.cn; 2020223060080@stu.scu.edu.cn).

Digital Object Identifier 10.1109/JSTARS.2021.3117946

In surface deformation analysis, despite the high accuracy of TLS and GB-SAR, their effective monitoring range may be limited due to topographic constraints [33]. Because the scanning position can only be set up where people can physically reach, it is sometimes difficult to obtain comprehensive terrain information in the presence of visual obstacles. In contrast, airborne UAV-based landslide monitoring has a wider field of vision, and it achieves accurate data alignment mainly by deploying a large number of ground control points (GCPs) [34]. Such GCPs are usually laid out according to handheld real-time kinematics (RTK) or global positioning systems, so their number and distribution determine the quality of the UAV data. However, in valleys, mountains, and dangerous disaster areas, it is sometimes unfeasible to set up sufficient manual GCPs in the study area, resulting in reduced accuracy of terrain data obtained by UAVs and inability to use multiphase terrain data for surface difference analysis. [35]. In addition to manual GCPs, another method to improve the accuracy of UAV data is post-processing kinematics (PPK), which can be used in the absence of manual GCPs. However, its accuracy is usually limited to getting topographic features or low-precision surface elevations, rather than high precision deformation analysis.

For early identification and dynamic monitoring of landslides, highly accurate and sensitive topographic data can provide powerful support for surface deformation analysis, disaster early warning, mechanism analysis, and risk assessment. With the rapid development of society and technological innovation, highways, tunnels, and bridges are gradually appearing in previously inaccessible mountain valleys. For these areas with complex terrain, the visual blindness of ground-based remote sensing technology is particularly evident. Furthermore, it is difficult to manually set up GCPs for airborne data collection as in plains or hilly areas, which poses a more serious challenge for landslide monitoring and prevention and control.

In this study, a method integrating TLS and UAV for landslide monitoring is proposed. This method combines the high accuracy of TLS and the flexibility of UAV and can quickly obtain a large range of high-precision terrain data for deformation analysis. This approach provides high-precision TLS-based GCPs (T-GCPs) for UAV photogrammetry, which can effectively improve the accuracy of UAV data and provide good support for data validation in places where manual GCPs cannot be set. In addition, the data acquired by these two remote sensing techniques can complement each other and can provide conditions for high-precision terrain modeling. The core of the method is to use the TLS point cloud data with millimeter-level accuracy as a fixed local coordinate system to provide an absolute reference for the generation, alignment, and deformation analysis of UAV data. Based on this fixed local reference system, researchers can densify the GCPs from the TLS point cloud and avoid setting up manual GCPs in complex terrain and hazardous environments, which greatly reduces the workload, cost, and danger. For mobilized landslides, this approach ensures the reliability and accuracy of the terrain data and reduces the potential risk of emergency treatment.

Based on this method, we analyzed the dynamic evolution of a reactivated ancient landslide, the Aniangzhai ancient landslide in Danba County, Southwest China. This ancient landslide was reactivated by the instability of the slope toe caused by the dam break flood of debris flow barrier lake in Xiaojinchuan River (XJC) on June 17, 2020. An early study was carried out in the emergency treatment of the reactivated ancient landslide on June 20, 2020 [36]. Although dozens of deformation monitoring points were set using GNSS and total stations, and two topographic difference maps of the reactivated ancient landslide were generated based on the satellite digital elevation model (DEM), the accuracy of the results and the monitoring range cannot fully reveal the mechanism of landslide initiation and movement, as well as the subsequent risk. Motivated by these early results, we carried out a half-year field investigation using TLS and UAV photogrammetry to expand the range and improve the accuracy of terrain data. Based on the integrating method, we have achieved the generation of high-precision UAV data in the absence of GCPs and realized centimeter-level surface deformation analysis (error of 0.5-2 pixels) of the visible slope as well as the visual blind spot. Moreover, based on 3D point cloud data and aerial orthophotos, the dynamic evolution and the reactivation mechanism of the ancient landslide were quantitatively analyzed through 2D and 3D methods. The purpose of this study is to provide a new perspective for the monitoring and management of mountainous disasters in complex terrain and offer basic data and guidance for follow-up research, hazard management, and disaster prevention for the reactivated Aniangzhai ancient landslide.

II. Background

A. Study Area

Danba County is located in the transition zone from the Qinghai-Tibet Plateau to the Sichuan Basin in Southwest China. Erosion and denudation landforms are fully developed in this area, with complex terrain, high mountains, steep slopes, and deep valleys [37]. The reactivation of ancient landslides is one of the important components of natural hazards in this region [38]. Earthquakes, rainfall, groundwater, erosion of slope toe, and increasingly frequent human activities have led to reactivation and slow deformation of the ancient landslides, resulting in ground cracking and the destruction of roads, farmland, and buildings [39]. Table I shows several reactivated ancient landslides in Danba County according to a geological hazard investigation report in 2004. Most of these ancient landslides are soil slopes formed by Quaternary deposits, with small slope angles and large volumes of soil mass. Because ancient landslides constitute one of the few relatively flat areas in Danba County, human activities nearby are frequent due to the suitable terrain and soil quality for living and farming. Many villages, towns, and even large cities are built on the top or at the foot of the ancient landslides, so the consequences of the reactivation of the ancient landslide could be catastrophic [40].

The reactivated Aniangzhai ancient landslide is located on the left bank of the XJC, approximately 19.5 km away from downstream Danba County (see Fig. 1). According to the engineering geological map [see Fig. 2(a)], the main strata of the Aniangzhai ancient landslide are the fourth formation of the

TABLE I
INVESTIGATED ANCIENT LANDSLIDES IN DANBA COUNTY

Ancient landslide	Latitude and longitude	Stratigraphic lithology	Average thickness (m)	Volume (10^4 m^3)
Danba downtown	E 101°52'43", N 30°53'12"	Q_4^{dl+cl}, $Q4^{fgl}$, Smx^4	30	220
Hongjun bridge 1#	E 101°53′50″, N 30°53′06″	$Q_4^{el+dl+cl}$, Smx^4	20	336
Hongjun bridge 2#	E 101°53′46″, N 30°52′58″	$Q_4^{el+dl+cl}$, Smx^4	20	330
Moluo	E 101°56′47″, N 30°51′16″	Q_4^{el+dl}, Smx^4	9	990
Haneyi	E 101°57′2″, N 30°54′04″	Q_4^{dl+cl}, Smx^4	15	12
Daxue	E 101°45′46″, N 30°56′15″	$Q_4^{el+dl+cl}$, Smx^4	14	1,078
Kayashan	E 101°59′30″, N 30°56′55″	Q_4^{el+dl}, Smx^5	10	330
Ganqiaogou	E 101°52'45", N 30°52'50"	$Q_4^{sef.}$, Sth^5	38	182
Yakeze	E 101°55′51″, N 30°51′24″	Q_4^{dl+cl}, Smx^4	15	110

Q_4^{el}, Q_4^{dl}, Q_4^{cl}, $Q_4^{sef.}$ and Q_4^{fgl} are Quaternary eluvium, diluvium, colluvium, debris flow deposit, and ice water deposit, respectively; Smx^4 is the fourth formation of the Silurian Maoxian Group; and Sth^5 is the fifth member of the Silurian Tonghua Group.

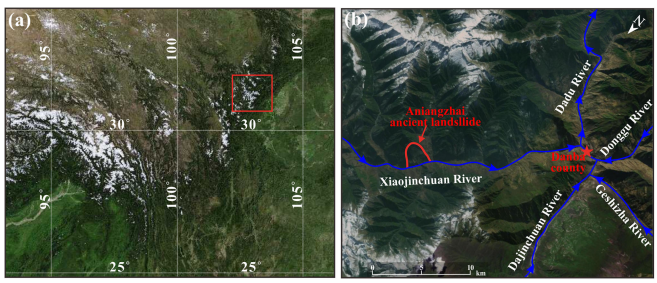

Fig. 1. Overview of the study area: (a) satellite image of the ancient landslide and (b) locality map of the study area.

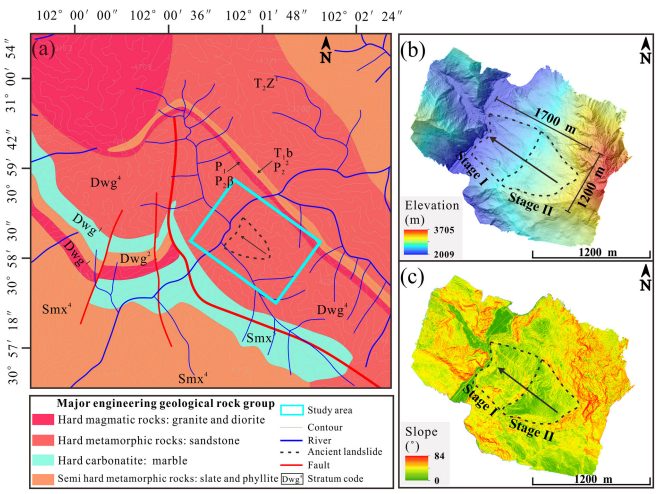

Fig. 2. Geological and topographical maps of the study area: (a) engineering geological map, (b) elevation map, and (c) slope map.

Paleozoic Devonian Weiguan group (Dwg^4), which mainly consist of silver–gray grayish biotite schist, gray–white quartzite, black carbonaceous slate, and gray–white marble.

The volume of the ancient landslide is massive. Based on the UAV photogrammetry, the digital surface model (DSM) and slope map of the study area are generated [see Fig. 2(b) and (c)]. The resolution of the DSM is 0.05 m with an error less than 1 pixel. The maximum elevation difference of the ancient landslide is approximately 1000 m, the maximum width along the river is approximately 1200 m and the maximum length perpendicular to the river is approximately 1700 m. In addition, the ancient landslide can be divided into two stages according to the slope angle [see Fig. 2(c)]. Stage II is the upper part of the ancient landslide (the visual blind spot), which is relatively flat with an average slope angle between 10° and 30°. Stage I is the lower part of the ancient landslide (the visible slope) with a steeper slope angle between 30° and 40°.

B. Danba "6.17" Debris Flow Disaster Chain

On June 17, 2020, a large debris flow occurred in Meilong gully under heavy rainfall. According to the Water Conservancy Bureau of Danba County, approximately 848 000 cubic meters of soils, sands, gravels, rocks, and boulders entered the main channel of XJC, leading to the blockage of the river channel and the formation of a debris flow-dammed lake [41]. Due to the large flow discharge in the flood season (from June to September), the debris flow dam failed quickly due to overtopping. As the result, the breakage of the debris flow dam formed a huge outburst flood, which flooded dozens of residential areas, farmland, and villages along the downstream river bank [see Fig. 3(a)]. Moreover, the strong impact and erosion of the dam break flood deeply disturbed the stability of the riverbed and slope toe of the Aiangzhai ancient landslide, resulting in the serious weakening of the antislide force of the left bank and the reactivation of the ancient landslide [see Fig. 3(b).

According to the cumulative deformation of the ancient landslide, five zones (I–V) of the slope are defined [see Fig. 3(a)]:

1) Zone I is the remnant back scrap of the slope toe caused by the dam break flood;
2) Zone II is in the middle part of stage I, with the largest cumulative deformation;
3) Zone III is located on the upstream side of zone II, with a cumulative deformation of approximately one-third of zone II;
4) Zone IV is located on the downstream side of zone II, with no obvious deformation;
5) Zone V is the entire stage II, with the cumulative deformation of approximately one-tenth of zone II.

III. METHODOLOGY AND MATERIAL

In this study, we used TLS and UAV for an on-site survey of the ancient landslide for half a year. The RTK and PPK were used to obtain initial geographical coordinates for TLS and UAV. After careful processing of the collected data, T-GCPs are extracted from the TLS point cloud for improvement and

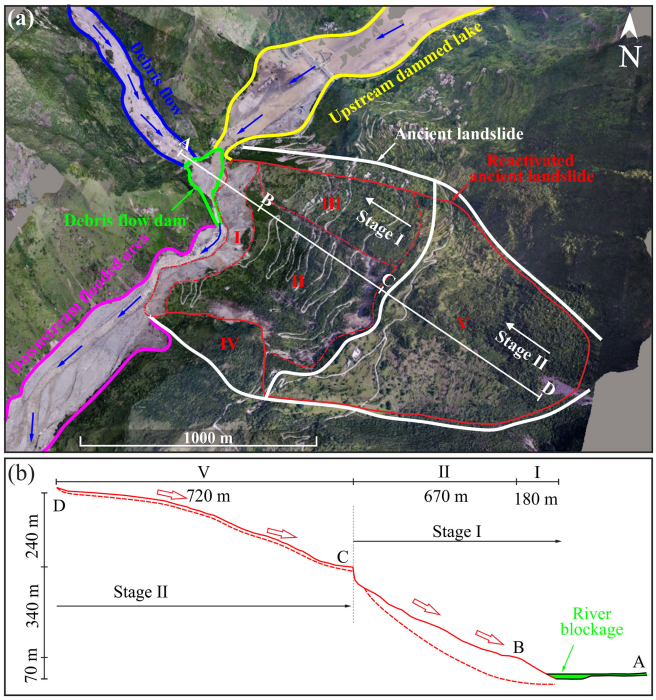

Fig. 3. Overview of the Danba "6.17" debris flow disaster chain. (a) Boundary of debris flow, flooded area, dammed lake, and ancient landslide is mapped based on on-site investigation and UAV 3D model. (b) Typical profile of the ancient landslide, and the depth of sliding surface is inferred according to bedrock exposure, riverbed disturbance, and slope erosion.

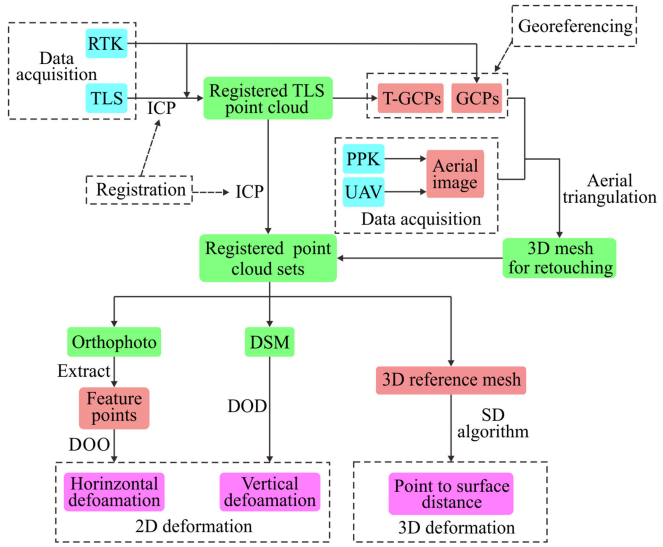

Fig. 4. Workflow of the study: The georeferencing and registration of UAV point cloud data are conducted by GCPs from RTK and TLS; the registration of point cloud is based on the ICP algorithm; and the deformation of landslides can be calculated by 2D and 3D methods for different failure patterns.

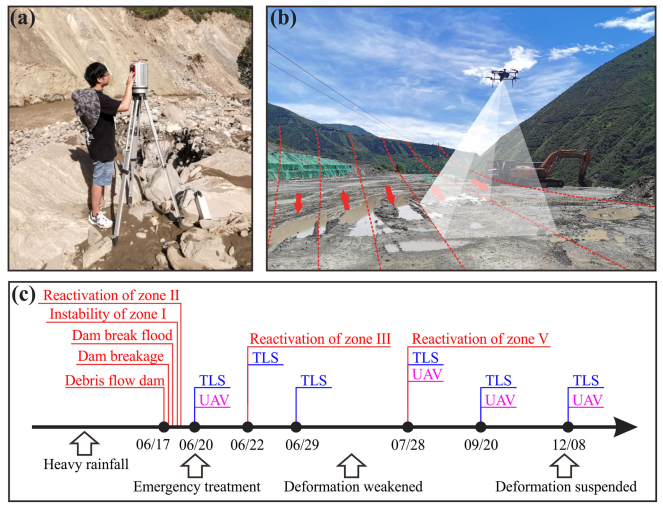

Fig. 5. On-site survey: (a) on-site TLS data acquisition, (b) on-site UAV aerial photo acquisition, and (c) chronological events of the reactivation of the Aniangzhai ancient landslide.

verification of UAV data. Then we use the iterative closest point (ICP) algorithm to register the point clouds obtained by TLS and UAV for deformation analysis. After that, we analyzed the deformation process of the ancient landslide through a variety of 2D and 3D methods, including the shortest distance (SD) method based on 3D point cloud, difference of DEM (DOD), and difference of orthophotos (DOO). The workflow of the methodology is shown in Fig. 4.

A. Data Acquisition

TLS and UAV were used for topography and terrain acquisition, as well as monitoring the evolution of reactivated ancient landslide [see Fig. 5(a)–(b)]. TLS is a remote sensing technology that uses laser beams to collect 3D spatial information from research targets in the environment [42]. TLS has strong stability, high precision, and strong penetration in vegetated areas. Compared to TLS, UAV photogrammetry generates 3D point clouds from 2D aerial images [43]. It is able to obtain a larger range of terrain information in a shorter period of time and its field of view is less restricted by the terrain. The 3D point cloud of UAV photogrammetry is obtained by aerial triangulation, which is a method of tie point densification that uses the intrinsic geometric characteristics of aerial photogrammetry. The principle of this method is to use overlapped aerial images and photogrammetric methods to build a flight route model or regional network model (optical or digital) corresponding to the field, and to obtain planar coordinates and elevations of densified point cloud sets [44]. In general, the accuracy and resolution of UAV aerial photography are less than that of TLS. In the absence of sufficient GCPs, the orthophoto, DSM and 3D models based on UAV photogrammetry may be distorted, and the elevation error (along z-axis) can reach several meters or even tens of meters [45].

In this study, the Riegl VZ-2000i (TLS) and FM-D2000 (UAV) were applied to acquire the terrain and topography. The RTK was used to set the basic GCPs for TLS, which processes carrier phase observations of two stations in real-time to obtain the geodetic coordinates of the ground [46]. The UAV-based PPK was applied to collect the initial position of each aerial image in the geographic coordinate system. Compared with RTK, PPK requires the use of software to solve the UAV coordinates

TABLE II
OVERVIEW OF TLS AND UAV DATA ACQUISITION

TLS-Riegl VZ-2000i			UAV-FM-D2000						
Scan mode	Angular resolution		Camera	Flight height	Flight mode	Average GSD	Images	Overlap	Sidelap
	Vertical	Horizontal							
Panorama	0.015 deg	0.015 deg	Sony D-op3000	300 m	Fixed flight height	0.05 m	570-600	>80%	>70%

GSD = ground sampling distance

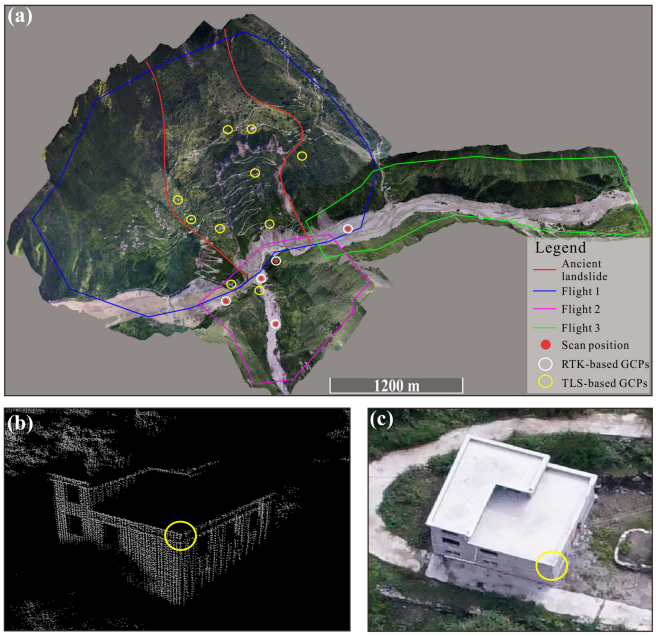

Fig. 6. Data acquisition: (a) the distribution and location of TLS and RTK scan position, and flight areas of UAV photogrammetry; (b)–(c) T-GCPs obtained from TLS data for aerial triangulation.

afterward, but its larger working radius and higher positioning frequency make it more suitable for UAV data collection. Fig. 5(c) shows the time series of the main events and data collection of the reactivated ancient landslide. In each period of the survey, we set five TLS scan positions along the XJC river and three flight areas of the study area [see Fig. 6(a)]. The details of the parameters setting of the TLS and UAV are shown in Table II.

B. Integration of TLS and UAV

To register the point cloud from TLS and UAV into an integrating point cloud data set, the ICP algorithm is applied in data registration. The processing of ICP algorithm in this study is based on the "plane patch filter" in the TLS processing software Riscan Pro for the Riegl VZ-2000i. This filter divides the point cloud into equal-sized cubes by an octree algorithm and repeatedly searches for planar areas (plane patches) by estimating the best-fit plane (least-squares method) from all points within the cube based on two major parameters, the "Maximum plane error" and "Minimum number of points per plane." The repetition is stopped if the standard deviation of the normal distances between all points and the planes is less than "Maximum plane error" or the number of points in the cube drops below the "Minimum number of points per plane." After that, the ICP algorithm selects the corresponding plane patches repeatedly and calculates the optimal rigid body transformation until it meets the convergence accuracy requirements of correct registration [47]. In order to obtain more detailed plane patches, the maximum plane error is set to 1.2 times the average spacing of the point clouds (0.05 m for TLS and 0.06 m for UAV), the minimum number of points per plane is set to 3, and the number of plane patches is approximately 1/20 of the total number of points in point cloud sets.

The core of TLS and UAV data integration is the registration of point cloud sets, which consists of three parts:

1) The registration of different TLS point cloud sets in one survey;
2) The registration of TLS point cloud sets from different surveys; and
3) The registration of point cloud sets from TLS and UAV photogrammetry.

In the registration of TLS data in one survey, six parameters, x, y, z, row, pitch, and yaw, are involved in the ICP algorithm. In general, the positions of scanner (x, y, and z) can be acquired by RTK, and its attitude (row pitch and yaw) can be determined by the internal compass. However, many errors in the process of data acquisition, such as RTK error, instrument tilt, and manual operation, will lead to errors in these six parameters. In order to solve this problem, we divide the ICP process into two steps, orientation adjustment and translation. The purpose of the orientation adjustment is to keep the X–Y plane of the point cloud coordinate system horizontal and to keep the *Y*-axis facing north. In this step, the error of RTK is ignored and its result is considered to be very accurate. Then, we lock the positions (x, y, z) of several point cloud sets (greater than or equal to 3) and rotate them to adjust row, pitch, and yaw. Such calculation results will make the point cloud coordinate system coincide with the global coordinate system as much as possible. The accuracy of this step is closely related to the accuracy of RTK. Then, we unlock the x, y, and z of some point cloud sets, and use the ICP algorithm again to adjust their spatial coordinates (the translation step). After repeating the above operations several times, we can realize the accurate registration of TLS data in one survey.

In the registration of TLS data from different surveys, we usually use the ICP algorithm to directly register one of the latest TLS scans with the early registered scans. This approach

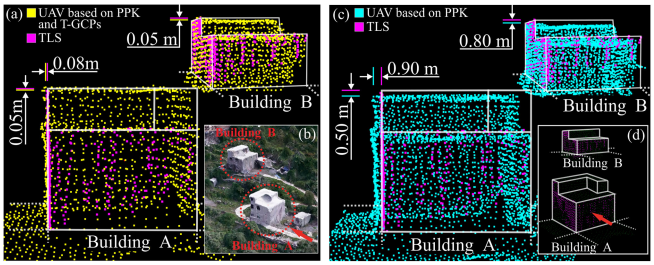

Fig. 7. Comparison of the UAV point clouds with (in yellow) and without (in blue) T-GCPs from TLS point clouds (in purple). (a) and (c) Side views along the direction of the red arrows in (b) and (d); the deviations in (a) and (c) are the average of the two point sets.

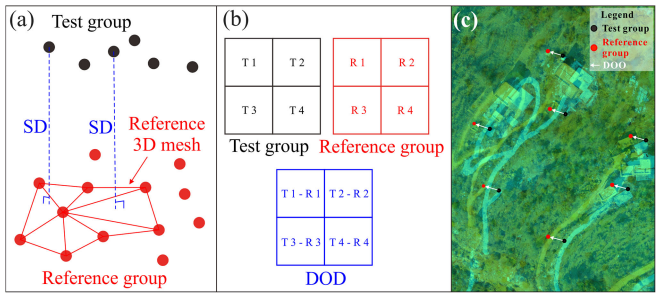

Fig. 8. Principle of the 2D and 3D deformation analysis method. (a) 3D deformation analysis method based on the SD algorithm. (b) 2D vertical displacement analysis method based on DOD. (c) 2D horizontal displacement analysis method based on DOO.

requires a large range of fixed overlapping areas between the new data and the early data, and there should be motionless objects in these areas, such as bedrock, boulders, bridges, and buildings. After completing the first registration of the latest TLS data, the other latest TLS data can be registered according to the first one.

After processing the TLS point cloud data, the next step focuses on the generation and registration of the UAV data. Since the point cloud sets are the core of TLS and UAV integration, the aerial triangulation that determines the density and accuracy of the UAV point clouds is of significant importance for the subsequent deformation analysis. The quality of aerial triangulation is largely affected by the accuracy, number, and distribution of GCPs, and the registration of TLS and UAVs data cannot meet the ideal level if the UAV point cloud data were twisted, stretched, or compressed due to the lack of GCPs [48]. In this study, except for the basic GCPs from RTK, we manually extracted obvious feature points, such as building corners, wire poles, or other landmarks as T-GCPs from the well-registered TLS data [see Fig. 6(b)–(c)]. As shown in Fig. 6(a), 5 basic GCPs were set along the XJC by RTK and 10 T-GCPs were extracted from TLS data.

The processing of UAV photogrammetry is based on the software ContextCaputre Master (CCM). This software enables aerial triangulation of aerial imagery, densification of point cloud, and generation of 2D orthophotos/DSM as well as 3D point clouds/models from aerial images. Besides, it allows users to produce and export the 3D mesh for retouching in a third-party software, which gives the convenience for the integration of TLS and UAV data. Therefore, after completing the aerial triangulation, we first generate 3D meshes for retouching, align them with the TLS point cloud using the ICP algorithm, and then reimport these 3D meshes into CCM for subsequent processing such as generation of orthophotos and point clouds.

Fig. 7 shows the comparison of UAV point cloud of two buildings in zone III with (yellow points) and without (blue points) T-GCPs. Both the UAV point cloud sets have been aligned with the TLS data (purple points) before comparison. The outlines of the buildings are depicted based on the TLS data, and then we adjust the viewpoint along the direction of the red arrow. The roof of Building B bends downward during the aerial triangulation, so we use the point cloud of the side walls in calculating the deviation. As a result, the integration of TLS can improve the accuracy of UAV point clouds from tens of pixels to 1–2 pixels (0.05–0.1 m). It also shows that the UAV point cloud without GCPs will be distorted or stretched due to the cumulative error of aerial triangulation, which cannot be calibrated by ICP algorithms.

C. Deformation Analyses

The key factor of deformation analyses is to find the spatial position of monitoring points before and after deformation. Commonly used single-point deformation monitoring devices such as GNSS can accurately record the spatial coordinates of monitoring points [9]–[11]. However, the high cost and complex field environment limit the number of such single-point monitoring devices, resulting in dispersed monitoring points that are unable to reflect the large-scale overall deformation.

The deformation analysis method based on TLS or UAV data is to superimpose the registered data from multiple periods and then calculate the differences by 2D or 3D methods. 3D deformation analysis methods are usually based on point clouds or 3D meshes to calculate the distance between the points in the test group (after deformation) and the reference group (before deformation). The common approach for 3D deformation analysis is to transform the reference point cloud data into 3D reference meshes through methods such as the least square method, quadratic function method, or Delaunay triangulation method and then calculate the SD from the test point to the 3D reference mesh to describe the 3D deformation [see Fig. 8(a)] [25], [33], [42]. The commonly used software for this method includes Geomagic Qualify and 3D Reshaper, etc. Besides, some methods can directly estimate the distance between two point cloud sets by the SD without 3D mesh generation, such as direct cloud-to-cloud comparison (C2C) [49] and multiscale model to model cloud comparison [50]. These methods have now been integrated into the 3D point cloud processing software CloudCompare. In this study, in order to reduce the interference of vegetation in the generation of 3D mesh, we used C2C in CloudCompare to analyze 3D deformation based on the point cloud. In general, the 3D deformation analysis methods mentioned above are nondirectional distance measurement methods that aim to find the SD between points (or 3D mesh), and they do not consider whether the direction of the SD is the true direction of deformation.

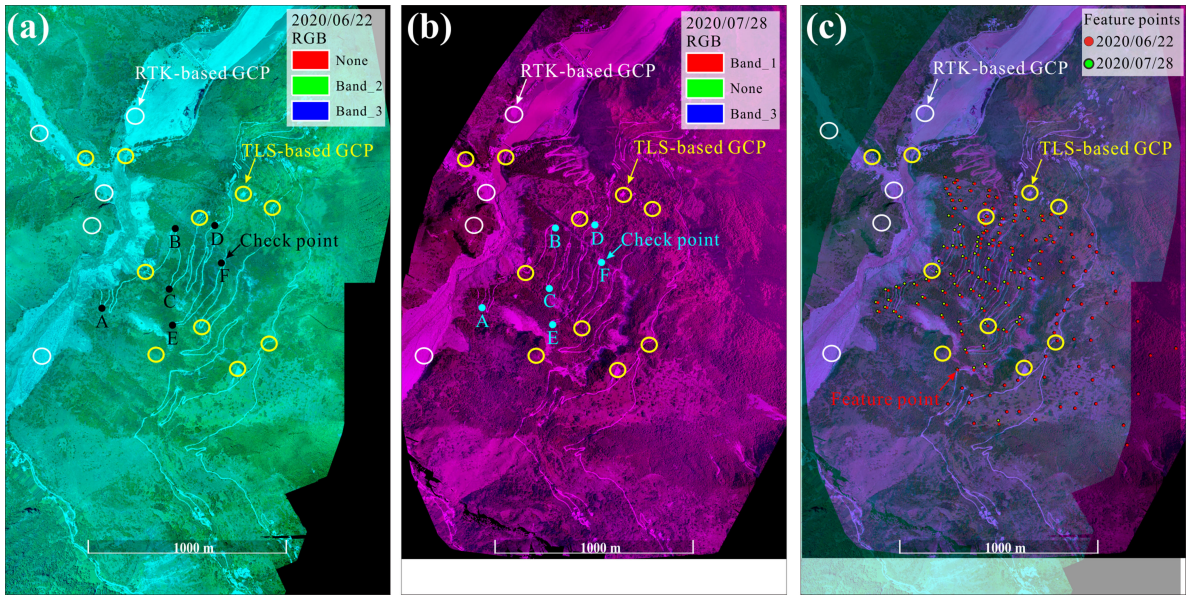

Fig. 9. Preparation of the DOO. (a) and (b) two orthophotos with different color bands, the checkpoints were selected for the accuracy assessment of DOO. (c) Superposition result of the pictures and feature points extracted according to distinguished landmarks.

Comparatively, 2D deformation analysis is a directional distance measurement method that only calculates the deformation along a certain direction, such as the vertical direction or horizontal direction. The DOD is a common vertical deformation measurement method that is often used to measure the subsidence of the ground [51]. This is a DEM-based or raster-based method to calculate the ground deformation vertically [see Fig. 8(b)].

Compared to DOD, DOO can calculate the horizontal deformation by extracting feature points in orthophotos and measuring the distance between these points [see Fig. 8(c)] [52]. These feature points can be extracted manually or calculated automatically by image recognition technology such as Harris corner detection. DOO is widely used in monitoring of slow ground movement, such as glacier and ice cap [27], [43], [51], [52]. In this study, we superimposed registered UAV orthophotos in different periods and changed their color bands to show the horizontal difference of the landslide [see Fig. 9(a)–(b)]. Then, according to the corner points of houses, roads, walls, large stones, and wire poles, we extracted 189 corresponding feature points in each of the UAV orthophotos [see Fig. 9(c)]. After that, the horizontal displacement of the ancient landslide was calculated, and the inverse distance weight method was used to interpolate the discrete horizontal distance.

D. Accuracy Assessment

The accuracy assessment of the integrating method includes: the registration of TLS point cloud, the quality of the UAV data, and the registration of UAV point cloud.

For the TLS point cloud, the ICP root mean square error (RMSE) of the raw data was affected by the deviation of noise and vegetation, resulting in large alignment errors. After filtering the noise and vegetation, the ICP RMSE for relatively smooth objects such as bedrocks, walls, bridges, and roads was approximately 3–5 mm. Table III shows the details of TLS point cloud data registration.

TABLE III
OVERVIEW OF THE TLS POINT CLOUD DATA REGISTRATION

Date	Scan positions	Registration reference	ICP RMSE(m)	
			Raw data	Filtered data
2020/6/20	5	GCPs from RTK	0.015	0.004
2020/6/22	5	TLS in 2020/6/20	0.013	0.005
2020/6/29	5	TLS in 2020/6/22	0.016	0.004
2020/7/28	5	TLS in 2020/6/29	0.012	0.003
2020/9/20	5	TLS in 2020/7/28	0.014	0.004
2020/12/8	5	TLS in 2020/9/20	0.013	0.005

In this study, the average ground sample distance is set to 0.05 m, and the resolution of the UAV data after aerial triangulation ranges from 0.047 to 0. 18 m. Then, we resampled the resolution of the orthophotos to 0.05 m. The sampling spacing of the point cloud data was set to 2 pixels, and the average point spacing was 0.1 m. The quality and registration of UAV data was evaluated by the GCPs error, which was obtained by comparing the GCP positions of orthophotos and DSM with those of RTK and TLS. Table IV shows the details of the accuracy assessment and registration of UAV data.

Moreover, in order to show the accuracy of the DOO and improvements of the integrated data, we conducted a comparative result only using RTK-based GCPs for aerial triangulation and selected 6 check points in the point cloud data for the accuracy assessment [see Fig. 9(a) and (b)]. The spatial coordinates of these check points were extracted and

TABLE IV
SUMMARY OF THE AERIAL TRIANGULATION ERRORS AND REGISTRATION OF UAV DATA

Aerial photogrammetry		Aerial triangulation errors-GCPs RMSE(m)				Registration		
Date	GCPs (RTK/TLS)	Resampled resolution (m)	RMSE - X(m)	RMSE -Y(m)	RMSE -Z(m)	Point spacing (m)	Registration reference	ICP RMSE(m)
2020/6/20	5/10	0.05	0.02	0.03	0.02	0.08 – 0.30	TLS in 2020/6/20	0.019
2020/7/28	5/10	0.05	0.05	0.03	0.03	0.08 – 0.32	TLS in 2020/7/28	0.018
2020/9/20	5/10	0.05	0.03	0.05	0.03	0.08 – 0.32	TLS in 2020/9/20	0.015
2020/12/8	5/10	0.05	0.04	0.04	0.03	0.08 – 0.36	TLS in 2020/12/8	0.016

TABLE V
ACCURACY ASSESSMENT OF DOO

Check points	Data source	Horizontal distance from the nearest GCP (m)	Displacement / Deviation (m)	
			Horizontal	Vertical
A	RD	-	3.098 / 0	-1.525 / 0
	ID	143	3.046 / -0.052	-1.463 / 0.062
	UD	328	3.025 / -0.073	-1.293 / 0.232
B	RD	-	4.001 / 0	-1.675 / 0
	ID	73	3.953 / -0.048	-1.634 / 0.041
	UD	385	3.889 / -0.112	-1.492 / 0.183
C	RD	-	3.412 / 0	-1.489 / 0
	ID	220	3.341 / -0.071	-1.461 / 0.028
	UD	427	3.288 / -0.124	-1.243 / 0.246
D	RD	-	3.228 / 0	-1.404 / 0
	ID	67	3.183 / -0.045	-1.341 / 0.063
	UD	451	3.115 / -0.113	-1.018 / 0.386
E	RD	-	3.122 / 0	-2.143 / 0
	ID	93	3.026 / -0.096	-2.073 / 0.07
	UD	617	2.976 / -0.146	-1.707 / 0.436
F	RD	-	4.418 / 0	-1.377 / 0
	ID	190	4.334 / -0.084	-1.299 / 0.078
	UD	554	4.256 / -0.162	-0.965 / 0.412

RD: real deformation based on TLS data;
ID: improved deformation (ID) based on UAV point cloud with GCPs from RTK and TLS;
UD: unimproved deformation (UD) based on UAV point cloud with GCPs from RTK.

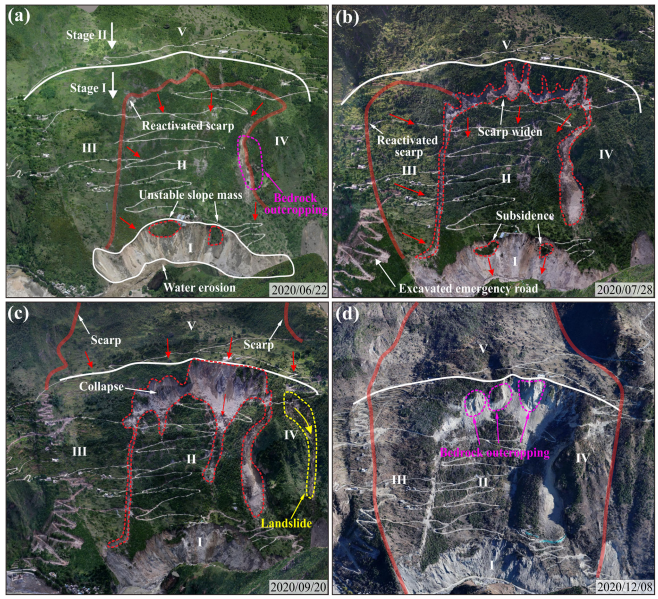

Fig. 10. Dynamic evolution of the reactivated Aniangzhai ancient landslide from 2020/06/22 to 2020/12/08 based on aerial photogrammetry. (a) About five days after the breakage of the barrier lake, obvious displacement occurred in zone II. (b) After large deformation in zone II, zone III began to slide towards zone II. (c) As stage I slid along the slope, stage II also began to slide down. (d) Ancient landslide tended to be stable after half a year.

the displacement were calculated and compared in Table V. It can be seen that the accuracy of UAV point cloud is related to the distance to the GCPs. The accuracy of UAV point cloud decreases with the distance of GCPs, and the error mainly appears in the vertical direction. It can thus be concluded that the integrating method can effectively reduce the aerial triangulation errors caused by the lack of sufficient GCPs.

IV. RESULTS

A. Overall Deformation

According to the 3-D model of UAV photogrammetry, the main movement mode of the reactivated ancient landslide was accompanied by extrusion deformation at the front and tension cracking at the back edge. The development of the reactivated ancient landslide can be divided into several steps according to the chronology (see Fig. 10).

a) The dam break flood caused strong erosion to the slope toe and riverbed, leading to the collapses in zone I.
b) Five days after the failure of zone I, obvious deformation and reactivated scarps were found at the back and upstream edges of zone II. In addition, small-scale landslides, collapses, and rockfalls continued to occur in zone I [see Fig. 10(a)].
c) Within one month, zone II experienced a major deformation, and the reactivated scarp expanded rapidly, resulting in the reactivation of zone III. Visible scarps appeared at the back and upstream edges of zone III [see Fig. 10(b)].
d) After two months, the reactivated scarps of zones II and III continued to expand. A large number of collapses occurred

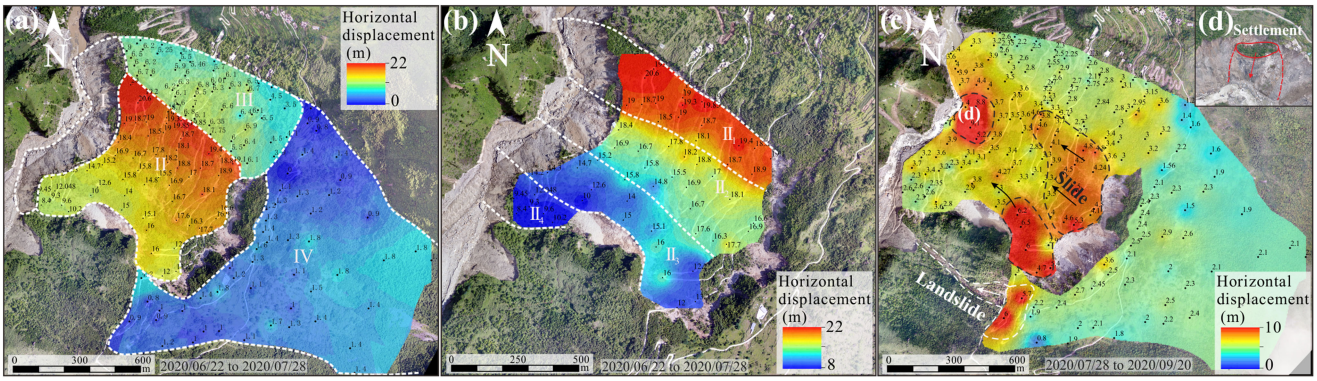

Fig. 11. Horizontal displacement of the whole ancient landslide based on DOO. (a) Horizontal displacement of the whole ancient landslide in the first month. (b) Horizontal displacement of zone II in the first month. (c) Horizontal displacement of the whole ancient landslide in the second and third months. (d) Local subsident of zone I.

on the slope toe of zone V, leading to further expansion of the reactivated scarp. Stage II underwent significant deformation, resulting in a newly reactivated scarp at its back edge. In addition, the outward deformation of stage II led to the formation of a small-scale landslide on the downstream side of its leading edge [see Fig. 10(c)].

e) At the end of 2020, the deformation of the ancient landslide tended to stop, and bedrock at the slope toe of stage II was exposed [see Fig. 10(d)].

B. Horizontal Displacement (DOO)

Fig. 11 shows the horizontal displacement of the reactivated ancient landslide according to DOO. In the first month after the reactivation [see Fig. 11(a)], the maximum horizontal displacements in zones II, III, and IV were approximately 20, 8 m, and 2 m, respectively. For zone I, due to continuous collapse and rockfall, the corresponding feature points before and after the deformation cannot be found in the first month, so the horizontal displacement in this area could not be analyzed by DOO. Compared with the first month, the deformation of the reactivated ancient landslide was obviously reduced in the next two months [see Fig. 11(c)]. The horizontal displacement of Stage I was between 2 and 4 m, and large displacements occurred in the back edge of zone II and the middle of zone I [see Fig. 11(d)] with displacements greater than 6 m. In addition, the horizontal displacement of Stage II was approximately 1–3 m, and a small-scale landslide occurred on its downstream side, with a maximum displacement of 6 m.

It is worth noting that the distribution of horizontal displacement of stage I was uneven in the first month, and it was strip-shaped and gradually decreased along the river. To further study this phenomenon, we subdivide zone II into four zones, II_1, II_2, II_3, and II_4, according to the horizontal displacement [see Fig. 11(b)]. The main reason for the reactivation of the ancient landslide was the reduction in anti-slide force caused by the instability of the slope toe and riverbed. Therefore, this strip-shaped deformation distribution showed a possibility that the instability of the slope toe or riverbed was different in severity along the river. The slope toe on the upstream side may be more severely disturbed, resulting in a horizontal displacement of more than 20 m in the first month.

C. Dynamic Evolution of the Slope Toe (SD)

Due to the continuous collapse in the first month and the failure of DOO deformation analysis, the dynamic evolution process of zone I was analyzed by the SD algorithm based on point cloud data for 3-D deformation.

First, we used four registered UAV point cloud datasets to analyze the deformation of zone I for the whole monitoring period (see Fig. 12). In the first month, zone I experienced large deformation, including collapse, outward deformation, and subsidence, with maximum deformation more than 10 m [see Fig. 12(a)]. In the next two months, except for local subsidence, zone I deformed outwards with a distance of approximately 2–5 m [see Fig. 12(b)]. This result is consistent with the result of DOO in Fig. 11(c). It is worth noting that the riverbed experienced obvious horizontal deformation and vertical uplift at this time, resulting in the narrowing of the river channel. In the last three months, the deformation of zone I tended to be stable, and the overall deformation was approximately 0–0.5 m [see Fig. 12(c)]. In addition, the deformation in upstream was obviously larger than that downstream, which corresponded to the strip-shaped horizontal displacement in Fig. 12(a) and (b).

According to a field investigation, the slope toe experienced a complicated deformation process in the first month. We did not collect enough UAV data in the first month, especially in the first 10 days after the disaster, because the continuous heavy rains prevented the drones from working. Therefore, we used four periods of TLS data in the first month to further analyze the dynamic evolution of the slope toe (see Fig. 13). Limited by the field of view, the TLS data only contained the slope toe corresponding to zones II_1 and II_2. In addition, the terrain of the riverbed cannot be obtained by TLS due to the high-level water. The results showed that the deformation of the slope toe could be divided into four types.

a) Collapse and rockfall: the slope toe was unstable due to the steep slope (70°–90°) and tensile cracks after the flood-induced landslide. The collapses and rockfalls gradually

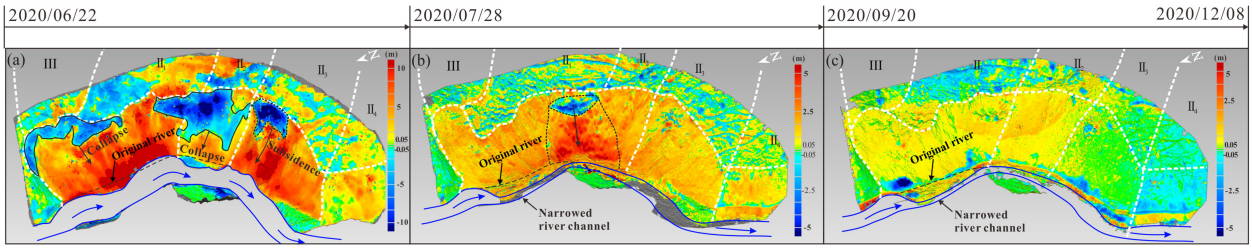

Fig. 12. Three-dimensional deformation analysis of the slope toe based on UAV point cloud data. (a) Three-dimensional deformation of the slope toe in the first month. (b) Three-dimensional deformation of the slope toe in the second and third months (c) Three-dimensional deformation of the slope toe in the last three months.

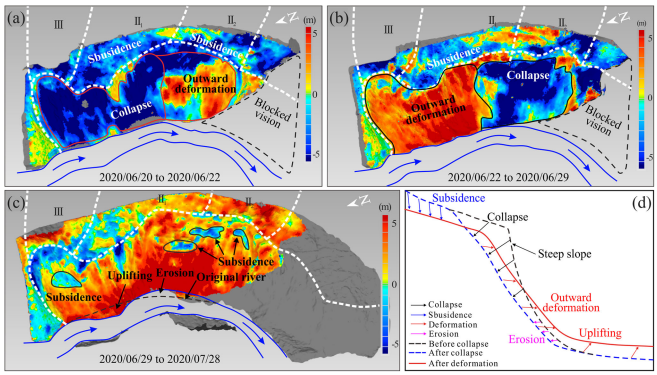

Fig. 13. Three-dimensional deformation analysis of the slope toe based on TLS point cloud data. (a) Three-dimensional deformation of the slope toe from 2020/06/20 to 2020/06/22. (b) Three-dimensional deformation of the slope toe from 2020/06/22 to 2020/06/29. (c) Three-dimensional deformation of the slope toe from 2020/06/29 to 2020/07/28. (d) Deformation mechanism of the slope toe.

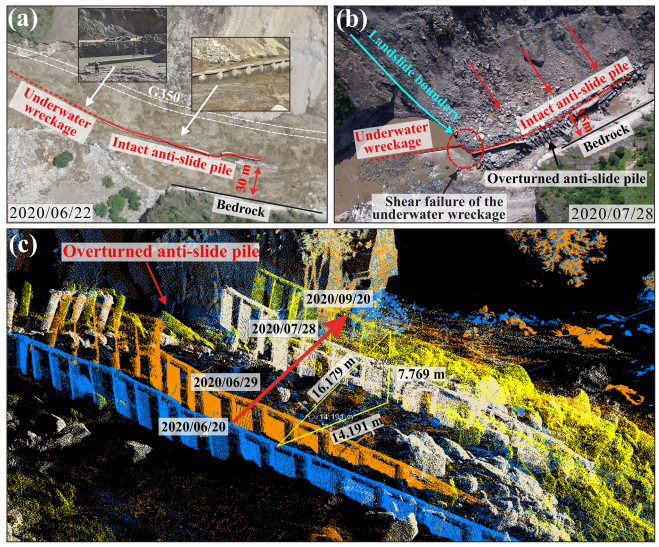

Fig. 14. Dynamic evolution of the riverbed based on on-site inversion and TLS data. (a) and (b) Deformation of the riverbed based on photographs. (c) Deformation of the riverbed based on TLS data.

occurred over time, which lasted for approximately 10 days [see Fig. 13(a)and (b)].

b) Outward deformation: the deformation direction of the slope varied spatially. The direction of the middle and upper part was mainly horizontal, while the direction of slope toe was upward.

c) Subsidence: subsidence was one of the main movement patterns of the reactivated ancient landslide, which was deformed along the slope due to the instability of the slope toe. The subsidence in zone I mainly occurred in the middle and upper parts of the slope [see Fig. 13(c)]. Since the deformation direction could not be distinguished by the SD algorithm, it was difficult to distinguish the subsidence from collapse in the first 10 days [see Fig. 13(a) and (b)].

d) Erosion to the slope toe: erosion to the slope toe mainly occurred at the bend of the river channel, which was the major factor triggering local subsidence. The slope toe without covering layer was easily eroded by running water. In addition, the residual debris dam partially blocked the river, resulting in the rise of the water level and aggravated erosion to the slope toe.

D. Reactivation Mechanism of the Ancient Landslide

The dynamic evolution of the slope toe in Figs. 12 and 13 explained the apparent reactivation of the ancient landslide but did not fully reveal the mechanism. Since reactivation of the ancient landslide is importantly associated with riverbed instability, the lack of riverbed topography in the TLS data makes it difficult to analyze the dynamic evolution of the riverbed in detail. Therefore, we supplemented the description of the riverbed development by analyzing the displacement of the anti-slide piles of G350 (see Fig. 14). The G350 is a national highway built along the foot of the ancient landslide. Part of its foundation (the anti-slide pile) was damaged by the flood-induced landslide, whereas the rest was well preserved [see Fig. 14(a)]. According to the aerial photographs in 2020/06/22 and 2020/07/28, the anti-slide pile experienced obvious horizontal deformation within one month, showing an approximately 15 m displacement towards the opposite bank. In addition to the horizontal displacement, the anti-slide pile also experienced apparent shear and toppling failure along the landslide boundary [see Fig. 14(b)]. Moreover, according to TLS data, we also found that the anti-slide pile had experienced a large uplift, with a height of 7.769 m in three months [see Fig. 14(c)].

To explain this phenomenon, we extracted the profiles of this area and illustrated the mechanism of the horizontal and upward deformation of the riverbed as well as the shear and

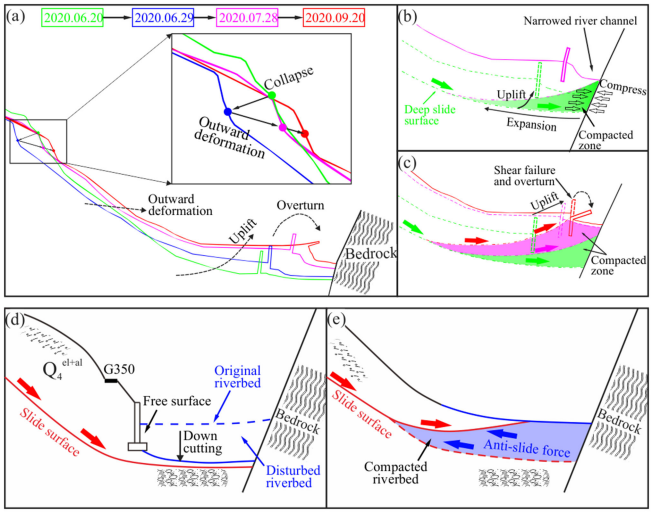

Fig. 15. Reactivation and evolution mechanism of the ancient landslide. (a) Dynamic evolution of the slope toe. (b) and (c) Evolution mechanism of the slope toe. (d) Reactivation mechanism of the ancient landslide. (e) Mechanism of gradual stabilization of the reactivated ancient landslide.

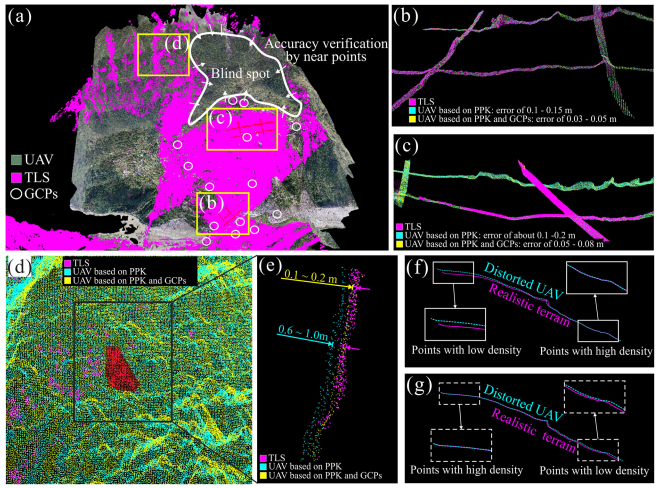

Fig. 16. Impact of GCPs on the distortion characteristics of UAV point cloud. The TLS point cloud data, and the UAV point cloud based on PPK and GCPs (including GCPs from RTK and TLS) were compared after registration. (a) Distribution of TLS/UAV point cloud, it shows the location of visual blind spot. Two different kinds of UAV point cloud data were used, the PPK-based and PPK/GCPs-based. (b) and (c) Several profiles with good alignment in the dense point cloud of the three kinds of point clouds. (d) and (e) Poorly aligned sparse point clouds when the UAV data are distorted. (f) and (g) Distortion principle of the UAV point cloud. (f) Same as the actual situation.

toppling failure of the anti-slide piles [see Fig. 15(a)]. At first, the horizontal displacement of the anti-slide pile on the riverbed indicated that the sliding surface of the ancient landslide was deep, leading to simultaneous movement of the anti-slip piles and the riverbed. Due to the existence of bedrock on the opposite bank, the horizontal displacement of the riverbed was constrained. With the continuous accumulation and compression of landslide materials at the junction of the riverbed and opposite bedrock, the riverbed gradually becomes dense from bottom upwards, resulting in the uplift of the sliding surface and the riverbed [see Fig. 15(b)]. With the development of the compression effect, the exit of the sliding surface gradually transferred toward the slope, and the anti-slide pile would topple and overturn due to the horizontal thrust when the exit of the sliding surface reached the back of the anti-slide pile [see Fig. 15(c)]. Therefore, the main reason for the reactivation of the ancient landslide was the erosion and downcutting of the riverbed by the dam break flood, which led to the formation of free surfaces and the reduction of anti-slide force at the foot of slope [see Fig. 15(d)]. With the densification of the riverbed and the increase in the anti-sliding force, the deformation of the ancient landslide gradually slowed down [see Fig. 15(e)].

V. Discussion

In this study, the quantitative monitoring of the reactivated ancient landslide is based on the integration of TLS technology and UAV photogrammetry, which has wide application prospects in mountain disaster monitoring and management. UAV aerial photogrammetry has a wide field of vision and can collect terrain and topography quickly, but it is unable to effectively account for the elevation of the ground. In the absence of GCPs, UAV data are prone to compression, stretching, and distortion. In mountainous areas with complex terrain, the dense vegetation, steep slopes and lack of roads in can limit the amount and accuracy of manual GCPs. Coupled with the huge height differences in high mountain valleys, errors in UAV data can increase rapidly, especially in the Z-direction, which can reach several meters. In this study, the high accuracy of TLS can provide sufficient T-GCPs, reference and common areas for the generation, registration, and verification of UAV point cloud sets, which is very helpful for studying large high and steep slopes as well as dangerous areas that are inaccessible to field crews. Therefore, the integration of the two remote sensing technologies can improve the convenience, extensiveness, and accuracy of terrain information acquisition.

In contrast, although the PPK-based UAV data acquisition method is widely used, its accuracy of a few centimeters or tens of centimeters can only be used to collect topographic features and DSM with low accuracy, which is not suitable for high-precision ground deformation analysis. As shown in Fig. 16, the accuracy of UAV point cloud data based on PPK and PPK/GCPs is compared. The result shows the errors and distortion characteristics of the UAV point cloud in the absence of GCPs. Since the basic principle of the ICP algorithm is the least-squares method, which uses the minimization of the sum of squares of the errors to find the best functional match of the data. Therefore, areas with high point density and low distortion will be prioritized for registration in the ICP algorithm. In contrast, the areas with low point density or large errors will show poor alignment results [see Fig. 16(f) and (g)]. For the distorted PPK-based UAV point cloud in this study, the ICP algorithm gives priority to the high-density point cloud at the foot of the slope, resulting in a large deviation from the sparse point cloud at the top of the mountain [see Fig. 16(f)]. In addition, the good registration of GCP-based UAV point clouds in Fig. 16(b)—(e) further demonstrates the significant positive effect of TLS on

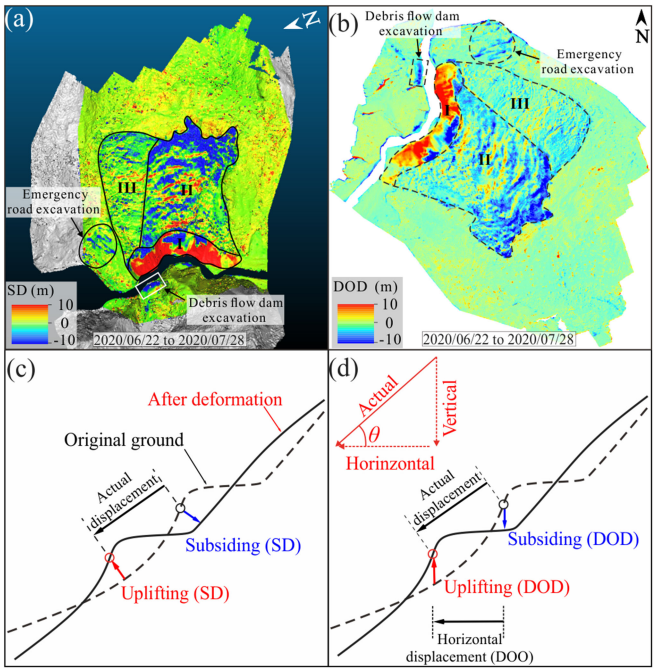

Fig. 17. Errors caused in the deformation analysis of the ancient landslide based on SD and DOD. (a) and (b) Results of deformation analyses based on SD and DOD. (c) and (d) Cause of the error in SD and DOD.

improving UAV data quality as well as the good accuracy of UAV point clouds in visual blind spot.

In this article, although DOO, DOD, and the 3-D deformation analysis method (SD algorithm) were introduced, we only used DOO to quantitatively calculate the horizontal displacement to reflect the actual deformation of the whole ancient landslide. This is because the DOD and SD are unable to accurately reflect the real deformation of the ancient landslide. Fig. 17(a) and (b) shows the results of the overall deformation of the ancient landslide based on SD and DOD, respectively. It can be observed that the deformation of stage I has a staggered distribution of uplift (red) and subsidence (blue) along the slope surface, which apparently cannot reflect the real movement of the whole ancient landslide. Fig. 17(c) and (d) illustrates the reasons for this situation. Since the direction of the ancient landslide is downward along the slope, the corresponding feature points before and after deformation defined by DOD and SD are not the same, so the results can neither represent the horizontal nor the vertical displacement. In contrast, although DOO only reflects the horizontal displacement of the landslide, it calculates the displacement according to the real distance of a feature point before and after deformation. Therefore, the horizontal displacement calculated by DOO is synchronous with the real deformation. Nevertheless, DOD and SD still have significant advantages in the study of landslides in that they can quickly and comprehensively identify the location, extent, or degree of the mobilized area. This is of great benefit to the fields of slope stability analysis, emergency treatment, and safety evaluation.

The identification of feature points before and after deformation is the key factor affecting the results of DOO. Scambos [52] used small-scale glacier surface features as markers of moving ice and used a cross-correlation algorithm to match the glacier displacement before and after the deformation to calculate the glacier velocity. Leprince [53] described a global scheme that iteratively refines a rough selection of GCPs such that the look direction correction implied allows for precise image georeferencing and coregistration. Bontemps [54] used the redundancy of displacement fields from image pairs to derive a robust time series of displacement of slow-moving landslides. Similar to DOO, these methods are based on feature points or land markers for deformation analysis. However, the application of these methods is limited when there are large changes in terrain features, such as rock avalanches, rapid landslides, or collapses, making it difficult to find the corresponding feature points before and after deformation. Therefore, DOO is more suitable for the analysis of slow moving or uniformly deformed ground.

VI. Conclusion

The integration of TLS and UAV technology effectively improves the range and accuracy of terrain data, which provides a strong contribution to mountain disaster management. The alignment of TLS and UAV point cloud data includes three parts: the registration of TLS data in one survey and different surveys, and the registration of TLS and UAV data. Two kinds of GCPs, the RTK-based and TLS-based, were used in aerial triangulation to improve the quality of the UAV point cloud. The ICP algorithm was applied in registration, and the maximum RMSE of TLS registration is 0.005 m, and the maximum RMSE of TLS and UAV registration is 0.019 m. The T-GCPs have proven to be effective in improving the accuracy of aerial triangulation, and thus the accuracy of deformation analysis.

According to the quantitative analysis, the main reason for the reactivation of the Aniangzhai ancient landslide is the instability of the slope toe and the riverbed caused by the dam break flood. The maximum deformation of the ancient landslide was approximately 26 m up to the last monitoring data. The main deformation of stage I was concentrated in the first month with a horizontal displacement of more than 20 m. The gradual densification of the disturbed riverbed and the increased anti-sliding force of the slope toe were responsible for the decrease of deformation rate.

For the sliding process along the slope, neither the 3-D deformation analysis based on the SD method nor the 2-D vertical deformation analysis based on DOD can effectively describe the process of landslide movement. Instead, because the horizontal displacement of the ancient landslide has a certain synchronization with the actual displacement, DOO can reflect the actual displacement to some degree. However, DOO is ineffective in cases where the ground surface is highly variable and can therefore only be used for slowly moving or uniformly deformed ground surfaces.

Acknowledgment

The authors would like to thank the anonymous reviewers for their time and constructive comments on the article.

REFERENCES

[1] F. Bozzano *et al.*, "Earthquake-reactivated landslide scenarios in southern Italy based on spectral-matching input analysis," *Bull. Earthq. Eng.*, vol. 11, pp. 1927–1948, 2013.

[2] D. M. Xue, T. B. Li, Y. X. Wei, and M. B. Gao, "Mechanism of reactivated Badu landslide in the Badu Mountain area, southwest China," *Environ. Earth Sci.*, vol. 73, pp. 4305–4312, 2015.

[3] J. W. Zhou, P. Cui, and M. H. Hao, "Comprehensive analyses of the initiation and entrainment processes of the 2000 Yigong catastrophic landslide in Tibet, China," *Landslides*, vol. 13, pp. 39–54, 2016.

[4] B. S. Park, H. Cho, S. P. Youn, and D. I. Park, "Analysis and evaluation of stability for the reactivated landslide along deep-seated weakness zones," *Geo-Eng.*, vol. 7, 2016, Art. no. 3.

[5] D. M. Gu, D. Huang, W. D. Yang, J. L. Zhu, and G. Y. Fu, "Understanding the triggering mechanism and possible kinematic evolution of a reactivated landslide in the Three Gorges reservoir," *Landslides*, vol. 14, pp. 2073–2087, 2017.

[6] K. He, G. T. Ma, X. W. Hu, and B. Liu, "Failure mechanism and stability analysis of a reactivated landslide occurrence in Yanyuan city, China," *Landslides*, vol. 18, pp. 1097–1114, 2021.

[7] W. L. Li *et al.*, "Deformation characteristics and failure mechanism of a reactivated landslide in Leidashi, Sichuan, China, on august 6, 2019: An emergency investigation report," *Landslides*, vol. 17, pp. 1405–1413, 2020.

[8] J. Guo, M. Xu, Q. Zhang, X. X. Xiao, S. S. Zhang, and S. M. He, "Reservoir regulation for control of an ancient landslide reactivated by water level fluctuations in Heishui river, China," *J. Earth Sci.*, vol. 31, pp. 1058–1067, 2020.

[9] Y. M. Zhang, X. L. Hu, D. D. Tannant, G. C. Zhang, and F. L. Tan, "Field monitoring and deformation characteristics of a landslide with piles in the Three Gorges Reservoir area," *Landslides*, vol. 15, pp. 581–592, 2018.

[10] D. Y. Li, L. X. Yan, L. Wu, K. L. Yin, and C. Leo, "The Hejiapingzi landslide in Weining county, Guizhou province, southwest China: A recent slow-moving landslide triggered by reservoir drawdown," *Landslides*, vol. 16, pp. 1353–1365, 2019.

[11] Z. N. Li, F. M. Zhang, W. Gu, and M. L. Dong, "The Niushou landslide in Nanjing city, Jiangsu province of China: A slow-moving landslide triggered by rainfall," *Landslides*, vol. 17, pp. 2603–2617, 2020.

[12] L. J. Lu, Y. Zhou, and R. T. Walker, "Using historical aerial photographs to measure earthquake deformation: Testing the effects of scan resolution," *Remote Sens. Environ.*, vol. 252, pp. 112–118, 2021.

[13] D. Raucoules, C. Maisons, C. Carnec, S. L. Mouelic, C. King, and S. Hosford, "Monitoring of slow ground deformation by ERS radar interferometry on the Vauvert Salt mine (France) comparison with ground-based measurement," *Remote Sens. Environ.,* vol. 88, pp. 468–478, 2003.

[14] H. F. Huang, J. J. Long, H. Y. Lin, L. Zhang, W. Yi, and B. J. Lei, "Unmanned aerial vehicle based remote sensing method for monitoring a steep mountainous slope in the Three Gorges Reservoir, China," *Earth. Sci. Inform.,* vol. 10, pp. 287–301, 2017.

[15] A. M. Booth, J. C. McCarley, and J. Nelson, "Multi-year, three-dimensional landslide surface deformation from repeat Lidar and response to precipitation: Mill gulch earthflow, California," *Landslides*, vol. 17, pp. 1283–1296, 2020.

[16] A. Serrano-Juan *et al.*, "Gb-SAR interferometry displacement measurements during dewatering in construction works. Case of la Sagrera railway station in Barcelona, Spain," *Eng. Geol.,* vol. 205, pp. 104–115, 2016.

[17] N. Jiang, H. B. Li, and J. W. Zhou, "Quantitative hazard analysis and mitigation measures of rockfall in a high-frequency rockfall region," *Bull. Eng. Geol. Environ.*, vol. 80, pp. 3439–3456, 2021.

[18] R. Zhao, Z. W. Li, G. C. Feng, Q. J. Wang, and J. Hu, "Monitoring surface deformation over permafrost with an improved SBAS-InSAR algorithm: With emphasis on climatic factors modeling," *Remote Sens. Environ.,* vol. 184, pp. 276–287, 2016.

[19] F. Biondi, P. Addabbo, C. Clemente, S. L. Ullo, and D. Orlando, "Monitoring of critical infrastructures by micromotion estimation: The Mosul dam destabilization," *IEEE. J. Sel. Topics Appl. Earth. Observ. Remote Sens.,* vol. 13, pp. 6337–6351, Oct. 2020.

[20] J. Dong, L. Zhang, M. S. Liao, and J. Y. Gong, "Improved correction of seasonal tropospheric delay in InSAR observations for landslide deformation monitoring," *Remote Sens. Environ.,* vol. 233, 2019, Art. no. 111370.

[21] J. Dong *et al.*, "Mapping landslide surface displacements with time series SAR interferometry by combining persistent and distributed scatterers: A case study of Jiaju landslide in Danba, China," *Remote Sens. Environ.,* vol. 205, pp. 180–198, 2018.

[22] A. Agapiou and V. Lysandrou, "Detecting displacements within archaeological sites in Cyprus after a 5.6 magnitude scale earthquake event through the hybrid pluggable processing pipeline (HyP3) cloud-based system and sentinel-1 interferometric synthetic aperture radar (InSAR) analysis," *IEEE. J. Sel. Topics Appl. Earth. Observ. Remote Sens.,* vol. 13, pp. 6115–6123, Oct. 2020.

[23] N. Casagli *et al.*, "Spaceborne, UAV and ground-based remote sensing techniques for landslide mapping, monitoring and early warning," *Geoenviron. Disasters*, vol. 4, 2017, Art. no. 9.

[24] H. B. Li, X. G. Yang, H. L. Sun, S. C. Qi, and J. W. Zhou, "Monitoring of displacement evolution during the pre-failure stage of a rock block using ground-based radar interferometry," *Landslides*, vol. 16, pp. 1721–1730, 2019.

[25] H. B. Li, X. W. Li, W. Z. Li, S. L. Zhang, and J. W. Zhou, "Quantitative assessment for the rockfall hazard in a post-earthquake high rock slope using terrestrial laser scanning," *Eng. Geol.,* vol. 248, pp. 1–13, 2019.

[26] N. Jiang, H. B. Li, M. S. Liu, J. Y. Zhang, and J. W. Zhou, "Quantitative hazard assessment of rockfall and optimization strategy for protection systems of the Huashiya cliff, southwest China," *Geomat. Nature Hazard Risk*, vol. 11, no. 1, pp. 1939–1965, 2020.

[27] T. Li, B. G. Zhang, W. Xiao, X. Cheng, Z. H. Li, and J. Zhao, "UAV-based photogrammetry and LiDAR for the characterization of ice morphology evolution," *IEEE. J. Sel. Topics Appl. Earth. Observ. Remote Sens.,* vol. 13, pp. 4188–4199, Jul. 2020.

[28] R. Eker, A. Aydın, and J. Hübl, "Unmanned aerial vehicle (UAV)-based monitoring of a landslide: Gallenzerkogel landslide (Ybbs-Lower Austria) case study," *Environ. Monitoring Assessment,* vol. 190, 2018, Art. no. 28.

[29] R. Liu, L. Y. Li, S. Pirasteh, Z. L. Lai, X. Yang, and H. Shahabi, "The performance quality of LR, SVM, and RF for earthquake-induced landslides susceptibility mapping incorporating remote sensing imagery," *Arab. J. Geosci.,* vol. 14, 2021, Art. no. 259.

[30] C. M. Ye *et al.*, "Landslide detection of hyperspectral remote sensing data based on deep learning with constrains," *IEEE. J. Sel. Topics Appl. Earth. Observ. Remote Sens.,* vol. 12, no. 12, pp. 5047–5060, Dec. 2019.

[31] Q. Zhu, L. Chen, H. Hu, S. Pirasteh, H. F. Li, and X. Xie, "Unsupervised feature learning to improve transferability of landslide susceptibility representations," *IEEE. J. Sel. Topics Appl. Earth. Observ. Remote Sens.,* vol. 13, pp. 3917–3930, 2020.

[32] S. Pirasteh1 and J. Li, "Developing an algorithm for automated geometric analysis and classification of landslides incorporating Lidar-derived DEM," *Environ. Earth Sci.,* vol. 77, 2018, Art. no. 414.

[33] R. G. Huang *et al.*, "An efficient method of monitoring slow-moving landslides with long-range terrestrial laser scanning: A case study of the Dashu landslide in the Three Gorges Reservoir region, China," *Landslides,* vol. 16, pp. 839–855, 2019.

[34] S. Arriola-Valverde, L. C. Villalobos-Avellán, K. Villagra-Mendoza, and R. Rimolo-Donadio, "Erosion quantification in runoff agriculture plots by multitemporal high-resolution UAS digital photogrammetry," *IEEE. J. Sel. Topics Appl. Earth. Observ. Remote Sens.,* vol. 13, pp. 6326–6336, 2020.

[35] Q. Xu, W. L. Li, Y. Z. Ju, X. J. Dong, and D. L. Peng, "Multitemporal UAV-based photogrammetry for landslide detection and monitoring in a large area: A case study in the Heifangtai terrace in the Loess plateau of China," *J. Mountain Sci.,* vol. 8, pp. 1826–1839, 2020.

[36] B. Zhao *et al.*, "Emergency response to the reactivated Aniangzhai landslide resulting from a rainstorm-triggered debris flow, Sichuan province, China," *Landslides*, vol. 18, pp. 1115–1130, 2021.

[37] H. Deng, L. Z. Wu, R. Q. Huang, X. G. Guo, and Q. He, "Formation of the Siwanli ancient landslide in the Dadu river, China," *Landslides*, vol. 14, pp. 385–394, 2017.

[38] J. M. Kong, Z. F. Chen, and S. Z. Song, "Occurrence conditions and process analysis on fluidization of valley type landslide: Example of the fluidization of landslide in Qiongshan ravine, Danba," *Wuhan Univ. J. Nature Sci.*, vol. 11, pp. 829–834, 2006.

[39] J. W. Zhou, M. Y. Jiao, H. G. Xing, X. Y. Yang, and Y. C. Yang, "A reliability analysis method for rock slope controlled by weak structural surface," *Geosci. J.*, vol. 21, pp. 453–467, 2017.

[40] R. Q. Huang, "Some catastrophic landslides since the twentieth century in the southwest of China," *Landslides,* vol. 6, pp. 69–81, 2009.

[41] Y. Yan *et al.*, "Seismic signal characteristics and interpretation of the 2020 '6.17' Danba landslide dam failure hazard chain process," *Landslides*, vol. 18, pp. 2175–2192, 2021. 10.1007/s10346-021-01657-x.

[42] M. Batur, O. Yilmaz, and H. Ozener, "A case study of deformation measurements of Istanbul land walls via terrestrial laser scanning," *IEEE. J. Sel. Topics Appl. Earth. Observ. Remote Sens.,* vol. 13, pp. 6362–6371, 2020.
[43] W. W. Immerzeel *et al.*, "High-resolution monitoring of Himalayan glacier dynamics using unmanned aerial vehicles," *Remote Sens. Environ.,* vol. 150, pp. 93–103, 2014.
[44] J. C. Trujillo, R. Munguía, E. Ruiz-Velázquez, and B. Castillo-Toledo, "A cooperative aerial robotic approach for tracking and estimating the 3D position of a moving object by using pseudo-stereo vision," *J. Intell. Robot. Syst.*, vol. 96, pp. 297–313, 2019.
[45] P. D. A. Kraaijenbrink, J. M. Shea, F. Pellicciotti, S. M. de Jong, and W. W. Immerzeel, "Object-based analysis of unmanned aerial vehicle imagery to map and characterise surface features on a debris-covered glacier," *Remote Sens. Environ.,* vol. 186, pp. 581–595, 2016.
[46] U. Kizil and L. Tisor, "Evaluation of RTK-GPS and total station for applications in land surveying," *J. Earth. Syst. Sci.*, vol. 120, pp. 215–222, 2011.
[47] C. Fotsing, N. Menadjou, and C. Bobda, "Iterative closest point for accurate plane detection in unorganized point clouds," *Automat. Construction,* vol. 125, 2021, Art. no. 103610.
[48] B. O. Kim, K. H. Yun, and C. K. Lee, "The use of elevation adjusted ground control points for aerial triangulation in coastal areas," *KSCE. J. Civ. Eng.*, vol. 18, pp. 1825–1830, 2014.
[49] B. Jafari, A. Khaloo, and D. Lattanzi, "Deformation tracking in 3D point clouds via statistical sampling of direct cloud-to-cloud distances," *J. Nondestructive Eval.,* vol. 36, 2017, Art. no. 65.
[50] D. Lague, N. Brodu, and J. Leroux, "Accurate 3D comparison of complex topography with terrestrial laser scanner: Application to the Rangitikei canyon (N-Z)," *ISPRS J. Photogramm. Remote Sens.,* vol. 82, pp. 10–26, 2013.
[51] A. Kulshrestha, I. M. Bahuguna, B. P. Rathore, and K. V. Iyer, "Resolving biases in DEM differencing for estimation of change in elevation of glacier surfaces using Cartosat-i Stereo data," *J. Indian Soc. Remote Sens.*, vol. 48, pp. 1443–1453, 2020.
[52] T. A. Scambos, M. J. Dutkiewicz, J. C. Wilson, and R. A. Bindschadler, "Application of image cross-correlation to the measurement of glacier velocity using satellite image data," *Remote Sens. Environ.*, vol. 42, no. 3, pp. 177–186, 1992.
[53] S. Leprince, S. Barbot, F. Ayoub, and J. P. Avouac, "Automatic and precise orthorectification, coregistration, and subpixel correlation of satellite images, application to ground deformation measurements," *IEEE Trans. Geosci. Remote Sens.*, vol. 45, no. 6, pp. 1529–1558, Jun. 2007.
[54] N. Bontemps, P. Lacroix, and M. P. Doin, "Inversion of deformation fields time-series from optical images, and application to the long term kinematics of slow-moving landslides in Peru," *Remote Sens. Environ.*, vol. 210, pp. 144–158, 2018.

Nan Jiang received the B.S. and M.S. degrees in 2015 and 2021, respectively, from Sichuan University, Sichuan, China, where he is working toward the Ph.D. degree, all in water and civil engineering.

He worked as an Engineer with Sichuan University Engineering Design & Research Institute for two years after obtaining the B.S. degree in water and civil engineering. His main research interests include the remote sensing technologies and their application in identification and mitigation of natural hazards such as landslide and rockfall.

Haibo Li received B.S., M.S., and Ph.D. degrees in water and civil engineering from Sichuan University, Sichuan, China, in 2015, 2017 and 2020, respectively.

He works as a distinguished research fellow with Sichuan University after obtaining the Ph.D. degree. His main research interests include the integrated research and development of multisource noncontact monitoring technologies such as 3D laser scanning, ground-based synthetic aperture radar and UAV, and their application in engineering safety and geological disaster monitoring and early warning.

Yuxiang Hu received the B.S. degree the from Changsha University of Science and Technology, Changsha, China, in 2017, and the M.S. degree in 2020, from Sichuan University, Sichuan, China, where he is working toward the Ph.D. degree , all in water and civil engineering.

His research interests include geological disaster engineering and landslide dynamic simulation.

Jieyuan Zhang received the B.S. degree in 2019 from Sichuan University, Sichuan, China, where he is currently working toward the master's degree, both in water and civil engineering.

His research interests include the process and mechanism of the erosion and failure mechanism of landslide dam and landslide-dammed lake.

Wei Dai received the B.S. degree in 2020 in water and civil engineering from Sichuan University, Sichuan, China, where he is currently working toward the master's degree, both in water and civil engineering.

His research interests include the deformation monitoring of underground cavern and the identification of unstable rock mass.

Congjiang Li received the B.S. degree in 2020 from Sichuan University, Sichuan, China, where he is currently working toward the master's degree, both in water and civil engineering.

His research interests include the stability analysis of underground cavern and artificial slope.

Jia-Wen Zhou was born in Jiangxi, China in 1982. He received the M.S. and Ph.D. degrees in water and civil engineering from Hohai University, Nanjing, China in 2005 and 2008, respectively.

He is a Professor with the College of Water Resource and Hydropower of Sichuan University, Sichuan, China. He leads the team of engineering technology and disaster prevention of Sichuan University. His main research interests include monitoring, risk assessment, early warning, and emergency treatment of geologic hazards.

Dr. Zhou is the editorial board member of international journals such *Bulletin of Engineering Geology and the Environment* and *Journal of Mountain Science*.